PARTICLE-LADEN HYPOPYCNAL STRATIFIED SHEAR LAYER: LINEAR STABILITY ANALYSIS

Bruno Avila Farenzena, bruno.farenzena@acad.pucrs.br
Jorge Hugo Silvestrini, jorgehs@pucrs.br
Pontifcia Universidade Catlica do Rio Grande do Sul - PUCRS. Av. Ipiranga, 6681 Partenon - Porto Alegre-RS CEP: 90619-900

Abstract. *Gravity-driven riverine outflows are responsible for carrying sediments to the coastal waters, these flows generates some instabilities in the transport of river fresh water into the salty water like the Kelvin-Helmholtz and Holmboe. Results from temporal linear stability analysis of a two layer stratified flow are presented, investigating the behavior of settling particles on the stability interface. The presence of settling particles have basically two effects in the flow: a variation in the Kelvin-Helmholtz mode, and the presence of a new growth mode. This new growth mode is characterized by a wavelength up to five times greater than the Kelvin-Helmholtz mode and can be the most amplified mode for some combination of parameters.*

Keywords: *Linear stability analysis, modal stability, particle-laden flows*

1. INTRODUCTION

Riverine outflows carry more than one-third of land-based precipitation to the oceans. The impact of the terrigenous material transported by these flows into the coastal waters depends on physical processes and transforms the river fresh water as it merges with salty water (Horner-Devine et al., 2015). This transformation process involves stratified-shear mixing caused by instabilities such as Kelvin-Helmholtz ($\mathcal{KH}$) and Holmboe ($\mathcal{H}$). These particle-laden flows are usually classified as hypopycnal plumes, resulting in a current along the top of the ocean, or hyperpycnal plumes, generating in a current that follows the bottom of the ocean known also as turbidity currents (Parsons et al., 2001) and are, often, modelled as stratified shear layers (Khavasi et al., 2014; Burns and Meiburg, 2012).

Most hydrodynamic stability studies in stratified shear layers do not consider the influence of settling particles in suspension. Betchov and Szewczyk (1963) performed a numerical study in the homogeneous shear-layer configuration and found that the Reynolds number, above some critical value, has no influence on the development of the $\mathcal{KH}$ instability allowing the inviscid fluid hypothesis in most of the linear stability works. Hazel (1972) conducted studies in stratified shear flows using the inviscid flow hypothesis and found critical values of Richardson number where the flow is stable and that the $\mathcal{H}$ instability can develop in any shear flow configuration as function of the ratio (R), defined as the relation between the shear layer thickness δ_u and the density layer thickness δ_ρ.

When the settling particles in suspension are considered, Khavasi et al. (2014) investigated the effect of bottom slope, viscosity and particle size in a particle-laden shear layer, where is characterized as a constant value of settling velocity modeled by the Stokes law (Julien, 1998). Among other results, the authors showed that the settling particles does not change the stability characteristics for dimensionless values of particle settling velocity smaller than 10^{-2}. For values greater than 10^{-2}, there is some changes in the instabilities that were not characterized. Based on this, the present study focuses in perform a linear stability analysis in a particle-laden flow where the main objective is the characterization of instabilities caused by settling particles.

This paper is organized as follows: at section 2 the flow configuration studied is presented; at 3 the governing equations are derived from the continuity, momentum and scalar transport equations; at 4 the numerical methods used to solve the governing equations are described; at 5 the developed computational code is validated; at 6 the results are presented; and lastly, at 7 contains the summary of results and the concluding remarks.

2. FLOW CONFIGURATION

We consider the stability of an unbounded fluid in a vertically stratified velocity and density profiles as sketched in Fig. 1. In this figure, the profile on the left side represents the streamwise velocity with minimum value u_{min}, maximum value u_{max} and shear layer thickness δ_u. The others velocities components are nulls. The profiles on the right side are the total density (solid line), the density added by sediment concentration (dash-dotted line) and the density added by salinity concentration (dashed line) where ρ_0 is the density of clear fluid (this means a fluid without sediment and salinity concentrations) and δ_ℓ (with $\ell = 1$ and 2) are layers thickness associated to the density added by sediment and salinity concentrations respectively.

The total density is assumed to be a linear function of sediment concentration φ_1 and salinity concentration φ_2:

$$\rho = \rho_0 \left(1 + \sum_{\ell=1}^{2} \gamma_\ell \varphi_\ell \right), \tag{1}$$

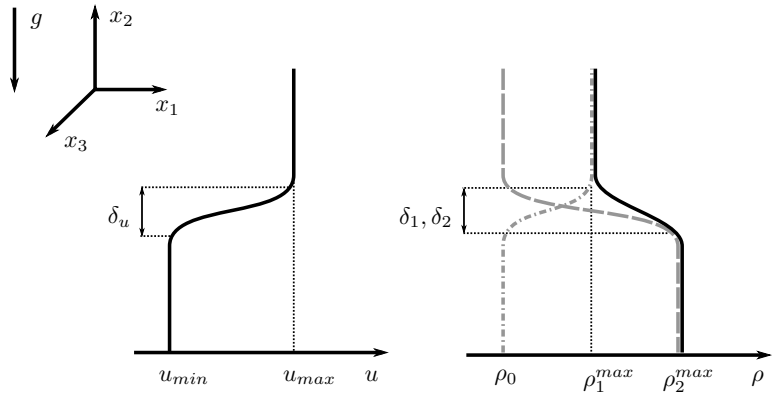

Figure 1. Flow configuration sketch. On the left side, the velocity distribution in the stream-wise direction. On the right side, the density distribution.

where γ_ℓ are the expansion coefficient. In this formulation, it is possible to observe that the values ρ_ℓ^{max} in Fig. 1 are defined by $\rho_0\gamma_\ell\varphi_\ell^{max}$.

We define a basic state of dimensionless velocity, sediment and salinity concentrations as follows:

$$\bar{u}_1(x_2) = a + \tanh(x_2), \tag{2}$$

$$\bar{\varphi}_1(x_2) = 1 + \tanh(R_1 x_2), \tag{3}$$

and

$$\bar{\varphi}_2(x_2) = 1 - \tanh(R_2 x_2), \tag{4}$$

where a is the a constant mean advection and $R_\ell = \delta_u/\delta_\ell$ is the ratio velocity shear layer thickness δ_u to a concentration thickness δ_ℓ. The profiles are made dimensionless by the use of the scales

$$U = \frac{\Delta u}{2}, \quad L = \frac{\delta_u}{2}, \quad \text{and} \quad \Phi_\ell = \frac{\varphi_\ell^{max}}{2} \tag{5}$$

with $\Delta u = u_{max} - u_{min}$. The choice of hyperbolic tangent for all basic state quantities is justified by a more direct comparison with previous studies results.

3. GOVERNING EQUATIONS

The study of small perturbations growing in the previously described flow configuration, via linear stability theory, requires linearised equations with explicit perturbation fields of flow quantities. These equations are obtained from the continuity, momentum and scalar transport equations by decomposing the flows quantities q_j in a steady part $\bar{q}_j$ (usually called as *basic state* or *base flow*) and in an unsteady part q'_j

$$q_j(x_k, t) = \bar{q}_j(x_k) + \varepsilon q'_j(x_k, t), \tag{6}$$

subtracting the equations for the steady flow and dropping the terms with ε^2 (Juniper et al., 2014). In Eq. (6), ε is a small valued constant. The resulting system of linearised equations from this proceeding, in its dimensionless form, is

$$\frac{\partial u'_j}{\partial x_j} = 0, \tag{7}$$

$$\frac{\partial u'_j}{\partial t} + u'_k\frac{\partial \bar{u}_j}{\partial x_k} + \bar{u}_k\frac{\partial u'_j}{\partial x_k} = \frac{1}{Re}\frac{\partial^2 u'_j}{\partial x_k \partial x_k} - \frac{\partial p'}{\partial x_j} + Ri_2\left(\frac{1}{R_\rho}\varphi'_1 + \varphi'_2\right)e_j^g, \tag{8}$$

$$\frac{\partial \varphi'_1}{\partial t} + u'_j\frac{\partial \bar{\varphi}_1}{\partial x_j} + \left(\bar{u}_j + u_s e_j^g\right)\frac{\partial \varphi'_1}{\partial x_j} = \frac{1}{ReSc_1}\frac{\partial^2 \varphi'_1}{\partial x_j \partial x_j} \tag{9}$$

and

$$\frac{\partial \varphi'_2}{\partial t} + u'_j\frac{\partial \bar{\varphi}_2}{\partial x_j} + \bar{u}_j\frac{\partial \varphi'_2}{\partial x_j} = \frac{1}{ReSc_2}\frac{\partial^2 \varphi'_2}{\partial x_j \partial x_j}, \tag{10}$$

where u_j is the fluid velocity, p the pressure, φ_ℓ a scalar concentration, x_k is the space coordinate, t is the time and e_j^g the unity vector in gravity direction, which in this case, is the $-x_2$ direction (Fig. 1). The dimensionless parameters are the Reynolds number (Re), salinity Richardson number (Ri_2), density ratio (R_ρ), Schmidt number (Sc_ℓ) and settling velocity of the particles (u_s). These dimensionless parameters are defined by:

- $$Re = \frac{\Delta u \delta_u}{4\nu}; \tag{11}$$
- $$Ri_2 = \frac{g\gamma_2 \delta_u \varphi_2^{max}}{\Delta u^2}; \tag{12}$$
- $$R_\rho = \frac{\gamma_2 \varphi_2^{max}}{\gamma_1 \varphi_1^{max}}; \tag{13}$$
- $$Sc_\ell = \frac{\nu}{\kappa_\ell}; \tag{14}$$
- $$u_s = \frac{2\tilde{u}_s}{\Delta u}. \tag{15}$$

The base flow is function of coordinate x_2 and, based on this, we may search a solution for the system of equation Eq. (7-10) using a perturbation in form of

$$q_j'(x_k, t) = \hat{q}_j(x_2) e^{i(\alpha x_1 + \beta x_3 - \sigma t)}, \tag{16}$$

where $\hat{q}_j$ is a amplitude function of a flow variable, α the streamwise wavenumber, β the spanwise wavenumber and σ is a complex number which its real part is the angular frequency and its imaginary part is the growth rate. This formulation of perturbation characterizes a temporal framework because α and β are real numbers and σ is a complex number.

Substituting the Eq. (16) in Eqs. (7-10), results in a eigenvalue problem where σ represents eigenvalues and the amplitude function of all flow variables are eigenvectors. With the objective of eliminate the pressure from the system of equations and reduce the size of the eigenvalue problem, one may use a formulation based on vertical vorticity component ($\hat{\omega}_2 = i\beta\hat{u}_1 - i\alpha\hat{u}_3$) described in the work of Schmid and Brandt (2014). This result in a generalized eigenvalue problem defined by:

$$i(\alpha\bar{u}_1 - \sigma)\hat{\omega}_2 + i\beta\frac{d\bar{u}_1}{dx_2}\hat{u}_2 = \frac{1}{Re}\mathcal{M}\hat{\omega}_2, \tag{17}$$

$$i(\alpha\bar{u}_1 - \sigma)\mathcal{M}\hat{u}_2 = -i\alpha\frac{d^2\bar{u}_1}{dx_2^2}\hat{u}_2 + \frac{1}{Re}\mathcal{M}^2\hat{u}_2 - Ri_2\,\tilde{k}^2\left(\frac{1}{R_\rho}\hat{\varphi}_1 + \hat{\varphi}_2\right), \tag{18}$$

$$i(\alpha\bar{u}_1 - \sigma)\hat{\varphi}_1 + \frac{d\bar{\varphi}_1}{dx_2}\hat{u}_2 - u_s\frac{d\hat{\varphi}_1}{dx_2} = \frac{1}{ReSc_1}\mathcal{M}\hat{\varphi}_1 \tag{19}$$

and

$$i(\alpha\bar{u}_1 - \sigma)\hat{\varphi}_2 + \frac{d\bar{\varphi}_\ell}{dx_2}\hat{u}_2 = \frac{1}{ReSc_2}\mathcal{M}\hat{\varphi}_2, \tag{20}$$

where $\mathcal{M}$ is the laplacian operator

$$\mathcal{M} = \frac{d^2}{dx_2^2} - \alpha^2 - \beta^2 \tag{21}$$

and $\tilde{k}$ is the total wavenumber

$$\tilde{k} = \sqrt{\alpha^2 + \beta^2}. \tag{22}$$

Considering a sufficiently large domain to avoid boundary perturbations, results in a Dirichlet boundary conditions for all amplitude functions in form of

$$\hat{q}_j(x_2^{min}) = \hat{q}_j(x_2^{max}) = 0. \tag{23}$$

4. NUMERICAL METHODS

To solve the generalized eigenvalue problem described by Eqs. (17-20) is necessary to discretize the spatial derivatives, transform the resulting grid and solve a discrete eigenvalue problem. Is chosen to do the spatial discretization the Chebyshev approximation (Canuto et al., 1988) based in the Chebyshev-Gauss-Lobato (CGL) collocation

$$\hat{y}_j = \cos\left(\frac{\pi j}{N}\right), \quad j = 0, 1, \ldots, N. \tag{24}$$

This differentiation method was implemented in a *Julia* code by adapting a *Differentiation Matrix Suite* routines developed by Weideman and Reddy (2000) in *Matlab* language.

As the CGL collocation corresponds to an orthogonal domain (from -1 to 1), it is necessary to transform the resulting grid into the physical coordinates. This can be done by the mapping function described by Berrut and Mittelmann (2004), it has the form

$$x_2 = \frac{m}{\theta}\tan\left[\text{atan}\left(\theta\right)\hat{y}\right], \tag{25}$$

where x_2 is the coordinate on the real domain, $\hat{y}$ is the CGL points, θ is the point density in a position, which in this case is $y = 0$, and m is the number of characteristics lengths necessary to truncate the domain. The parameter m must be sufficient large to not interfere in the instability development.

The differentiation matrix has also to be transformed to new coordinates by using the chain rule:

$$\mathcal{D} = \hat{\mathcal{D}}\frac{d\hat{y}}{dx_2}, \tag{26}$$

$$\mathcal{D}^2 = \hat{\mathcal{D}}^2\left(\frac{d\hat{y}}{dx_2}\right)^2 + \hat{\mathcal{D}}\frac{d^2\hat{y}}{dx_2^2} \tag{27}$$

and

$$\mathcal{D}^4 = \hat{\mathcal{D}}^4\left(\frac{d\hat{y}}{dx_2}\right)^4 + \hat{\mathcal{D}}^3\left(6\frac{d^2\hat{y}}{dx_2^2}\frac{d\hat{y}}{dx_2}\right) + \hat{\mathcal{D}}^2\left[3\left(\frac{d^2\hat{y}}{dx_2^2}\right)^2 + 4\frac{d^3\hat{y}}{dx_2^3}\frac{d\hat{y}}{dx_2}\right] + \hat{\mathcal{D}}\frac{d^4\hat{y}}{dx_2^4}, \tag{28}$$

where $\hat{\mathcal{D}}^n$ is the differentiation matrix in the orthogonal domain and $\mathcal{D}^n$ is the differentiation matrix in the real domain.

The resulting discrete eigenvalue problem is solved using the `eig` routine from *Julia* based on *Linear Algebra Package* (LAPACK) that applies the *QZ algorithm* (Anderson et al., 1999).

5. VALIDATION CASES

Two cases were chosen to validate the computational code: a homogeneous shear layer and a stratified shear layer. For the first case, the validation is based on the work of Betchov and Szewczyk (1963) and the *Squire's theorem* (Squire, 1933). This theorem, basically, says that in parallels flow for each three-dimensional perturbation exists a two-dimensional perturbation with greater growth rate. The second validation case is based on a comparison with analytical solutions available in Hazel (1972). Both validation cases considers null mean advection ($a = 0$), same layer thickness ratio ($R_\ell = 1$) and do not considers settling of particles ($u_s = 0$).

5.1 Homogeneous shear layer

This configuration is achieved, in the present formulation by setting $Ri_2 = 0$ or $R_\rho = 1$, it means that the total density profile is constant because both $R_\ell = 1$ and consequentially there is no density stratification. This section is organized as follows: a convergence test of growth rate with the mesh parameters N and θ, a verification of *Squire's theorem*, a verification of Reynolds number dependency and a comparison of maximum growth rate and most amplified wavenumber with results available on the literature.

The Fig. 2a shows the convergence of growth rate increasing the number of rid points. It is observed that the growth rate converges for approximatively 60 grid points. Figure 2b shows the convergence of growth rate increasing the point density parameter and we observe that the growth rate converges at $\theta = 30$. Based on these results, the growth rate is not affected by the mesh parameters N and θ when their values are greater than 60 and 30, respectively.

Figure 3 shows the growth rate isolines as a function of the spanwise and streamwise wavenumbers. The growth rate decreases with the increment of spanwise wavenumber while the maximum growth rates corresponds to $\beta = 0$, confirming the *Squire's theorem* in this configuration.

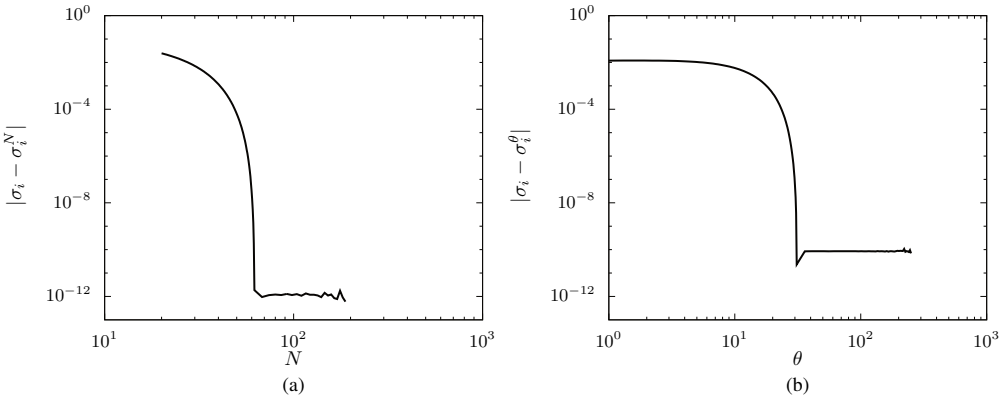

Figure 2. Convergence of σ_i increasing N (a), where σ_i^N is the growth rate for 200 points, and convergence of σ_i increasing θ (b), where σ_i^θ is the growth rate for $\theta = 300$.

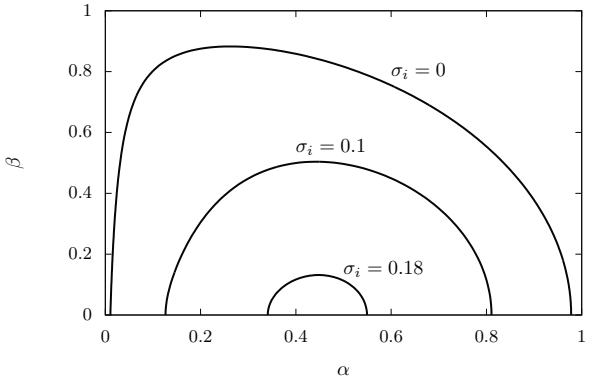

Figure 3. Growth rate isolines as function of α and β.

Figure 4 shows the behaviour of the growth rate and the most amplified wavenumber as a function of Reynolds number. It is observed that for a Reynolds number greater than 10^3, both the growth rate and the most amplified wavenumber are nearly constant reaching 99% of the value for $Re = 10^6$. This means that the viscous effects have no great influence in the development of this instability as it was verified in Betchov and Szewczyk (1963). The growth rate found for $Re = 10^6$ is 0.1897 with corresponding wavenumber of 0.4449. These results present a relative wavenumber error of $-6,74 \times 10^{-4}$ when compared with theory while the growth rate error is null.

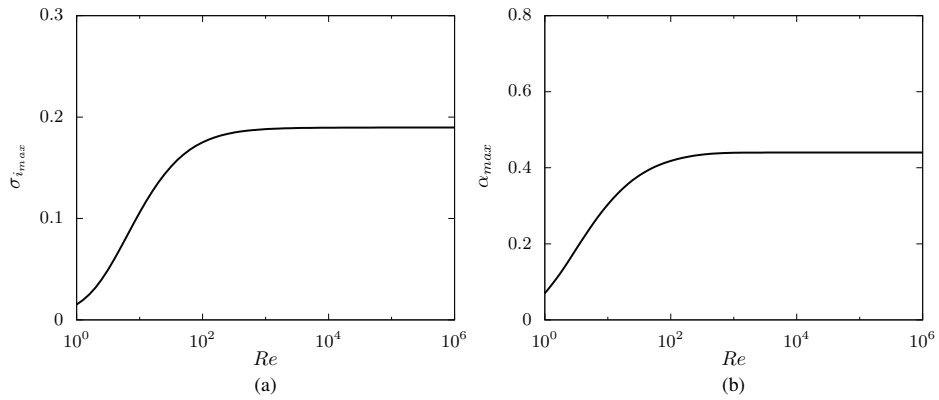

Figure 4. Maximum growth rate (a) and its corresponding wavenumber (b) as function of Reynolds number.

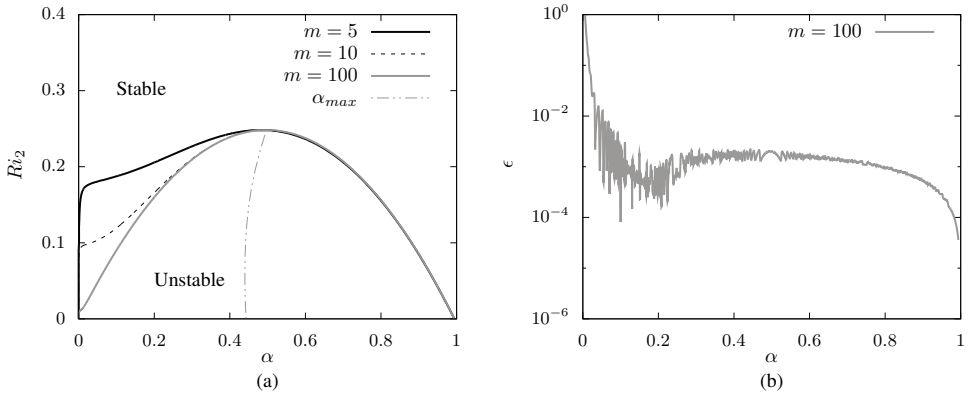

Figure 5. Stability boundaries (a) as a function of streamwise wavenumber and salinity Richardson number for different values of m and the relative error (b) between the stability boundary for $m = 100$ and the analytical solution, where α_{max} is the most amplified wavenumber.

5.2 Stratified shear layer

This configuration have a nonzero salinity Richardson number (Ri_2) and a density ratio (R_ρ) different than one. For hyperpycnal flows this parameter is lower than one and for hypopycnal flows is greater than one. For a better comparison with works available in the literature, R_ρ has to be sufficiently large. This analysis investigates the influence of domain truncation constant m in the stability boundary and results are compared with the analytical solution for inviscid flow ($Re \to \infty$) available in Hazel (1972): $Ri_{SB} = \alpha(1 - \alpha)$.

Figure 5a shows the stability boundary as function of wavenumber, salinity Richardson number and the domain truncation constant m considering a $Re = 10^3$. The stability boundary is deformed by the value of m but the most amplified wavenumber does not change. Figure 5b shows the relative error between the stability boundary for $m = 100$ and the analytical solution. This analytical solution has a critical Richardson number of 0.25 and the present study solution has a relative error of approximatively 10^{-3} of this critical number. Part of this error can be associated to the chosen Reynolds number for the homogeneous case, this value has a 1% growth rate error when compared to the inviscid flow growth rate.

In both validation cases, *Kelvin-Helmholtz* is the most amplified growth mode. In present study it will be called $\mathcal{KH}$ mode. $\mathcal{KH}$ mode is more amplified in the streamwise direction and characterized by a wavenumber between 0.4446 and 0.5, depending on the flow stratification, and a angular frequency with valued approximately two times greater than the dimensionless mean advection of the base flow (a). The angular frequency is not showed because the validation cases have a null mean advection.

6. RESULTS

Some problem parameters are fixed in order to reduce the complexity of the analysis, like the base flow parameters (a, R_1 and R_2), the Schmidt numbers of both scalar quantities and the Reynolds number. According Ortiz et al. (2002), the mean advection a in temporal framework acts as a Doppler shift in frequency affecting only the real part of σ, for this reason a is left as zero. The thickness ratio in both concentrations profiles are considered equals to 1 as the *Holmboe* instability is not considered (Hazel, 1972). Both Schmidt numbers are equals to 1 and the Reynolds adopted is 10^3. The parameters investigated are the streamwise wavenumber, the salinity Richardson number, the density ratio and the settling velocity.

Figure 6a shows the stability boundary as a function of salinity Richardson number and density ratio for a non-settling configuration and for some settling velocity values. It is observed that when the density ratio is sufficiently large the critical salinity Richardson number is 0.25 (same result as the second validation case). The increment of settling velocity makes the flow more unstable because it expands the unstable region.

Figure 6b shows the stability boundary as a function of streamwise wavenumber and density ratio for a non-settling and a settling configurations by considering a salinity Richardson number of 0.4. In this figure we observe another growth mode, caused by the presence of settling particles, for approximately $0 < \alpha < 0.25$. This new mode can be the most amplified mode for some combinations of settling velocity, density ratio and salinity Richardson number.

The predominance of this new mode due to the settling of particles can be observed in Fig. 7. Figure 7a shows the maximum growth rate as function of density for $Ri_2 = 0.4$, where we can see that the settling velocity must have a sufficiently large value to change the characteristic of the instability when compared with a non-settling condition. In this case, the settling velocity of 10^{-2} does not change the behaviour of the growth rate, but the value 2.5×10^{-2} it does with

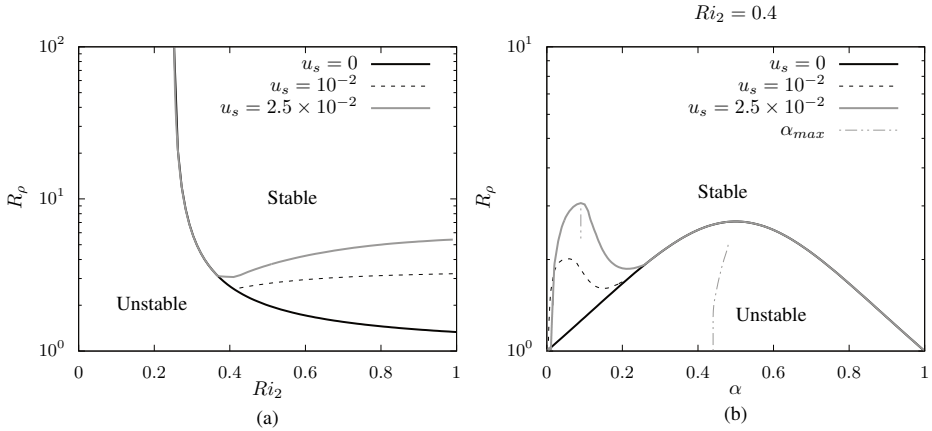

Figure 6. Stability boundary as a function of the salinity Richardson number and density ratio (a) and stability boundary as a function of the streamwise wavenumber and density ratio for $Ri_2 = 0.4$ (b), where α_{max} is the most amplified wavenumber for $u_s = 2.5 \times 10^{-2}$.

a different critical density ratio. Figure 7b presents the most amplified wavenumber as a function of the density ratio. The presence of this new growth mode, with characteristic wavenumber of approximatively 0.1 is responsible by the change of critical density ratio. Figure 7c shows the phase velocity, defined as

$$c = \frac{\sigma_r}{\alpha}, \tag{29}$$

as a function of the density ratio. It is observed that even small values of settling velocity changes this characteristic in $\mathcal{KH}$ instability and that the new mode has a characteristic phase velocity of -1. The discontinuities on the maximum wavenumber and phase velocity are caused by the change of most amplified growth mode.

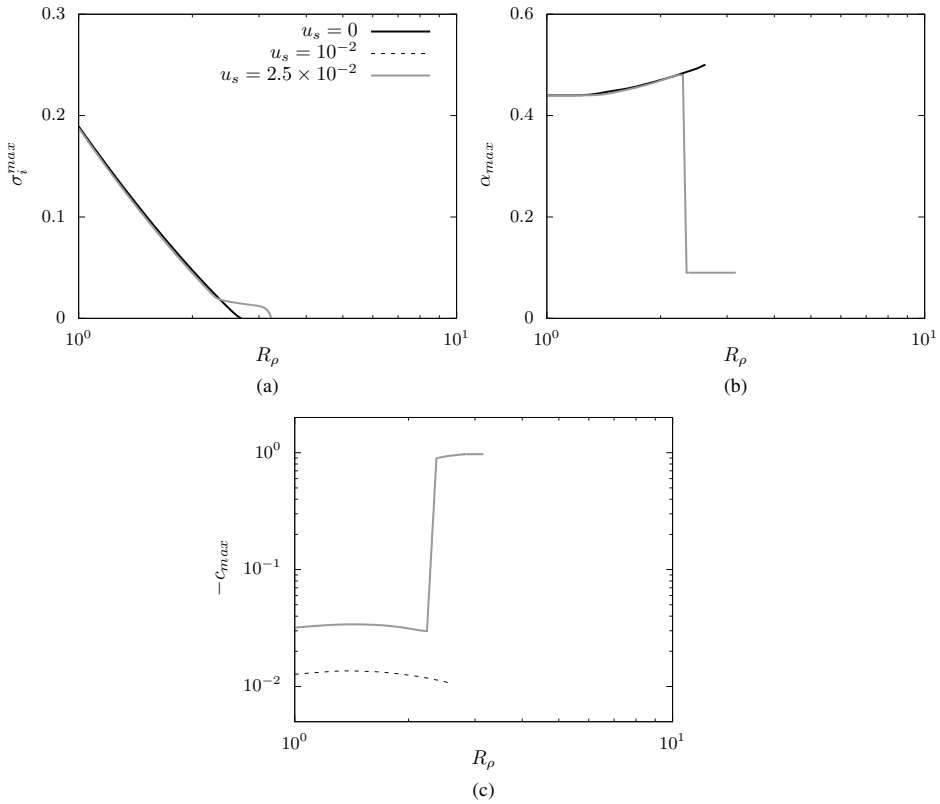

Figure 7. Maximum growth rate (a), most amplified wavenumber (b) and corresponding phase velocity (c) as a function of the density ratio. Results for $Ri_2 = 0.4$.

The presence of settling particles, in this flow configuration, can cause some changes in the $\mathcal{KH}$ mode and create another mode. Besides the variation in the phase velocity with the increment of u_s for the $\mathcal{KH}$ mode, it can be observed a deformation only in the sediment concentration perturbation field, presented in Fig. 8. In this figure, the solid black lines are positive isolines normalized between 0 and 1, the dashed gray lines are negative isolines normalized between -1 and 0, and the x_1 is normalized by it wavelength, defined as

$$\lambda = \frac{2\pi}{\alpha}. \tag{30}$$

These deformations cause by presence of settling particles can propitiate the development secondary instabilities but does not change the growth rate and the most amplified wavenumber.

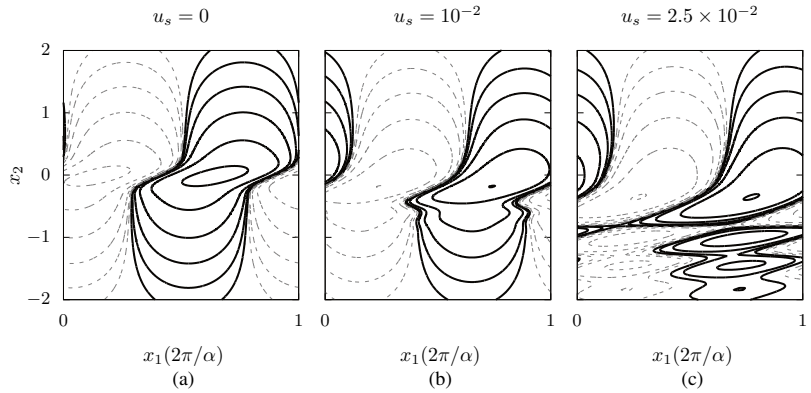

Figure 8. Sediment concentration perturbation field of $\mathcal{KH}$ mode as a function of the particles settling velocity.

Figure 9 shows perturbation fields of the streamwise velocity, the vertical velocity, the sediment concentration and the salinity concentration of the new mode, considering $u_s = 2.5 \times 10^{-2}$. In the same way as Fig. 8, the black solid lines are positive isolines normalized between 0 and 1, the gray dashed lines are negative isolines normalized between -1 and 0, and the x_1 is normalized by it wavelength. It is observed non-centered and non-symmetrical structures and a half wavelength displacement between the sediment concentration and the salinity concentration perturbation fields.

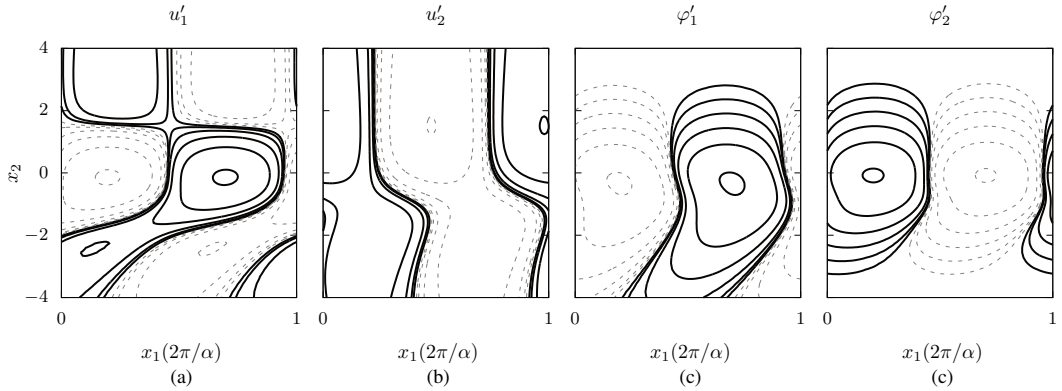

Figure 9. Perturbation fields of streamwise velocity (a), vertical velocity (b), sediment concentration (c) and salinity concentration (d) of the new mode.

Figure 10 shows a comparison of streamwise vorticity, defined as

$$\omega_3 = \frac{\partial u_2}{\partial x_1} - \frac{\partial u_1}{\partial x_2}, \tag{31}$$

between the $\mathcal{KH}$ mode and the new mode. Figure 10a and Fig. 10c are perturbation fields and Fig. 10b and Fig. 10d are total fields (base flow + perturbation fields) considering perturbation amplitude (ε from Eq. 6) of 0.5. Like the previous figures, the solid black lines are positive isolines normalized between 0 and 1, the dashed gray lines are negative isolines normalized between -1 and 0, and the x_1 is normalized by it wavelength.

In the $\mathcal{KH}$ mode, it is observed that the perturbation have the tendency of form vortex in the clockwise sense centered in the point of maximum vorticity ($x_2 = 0$). While in the new mode, it is observed the tendency of formation of counter-rotating vortex in approximately $x_2 = -1$.

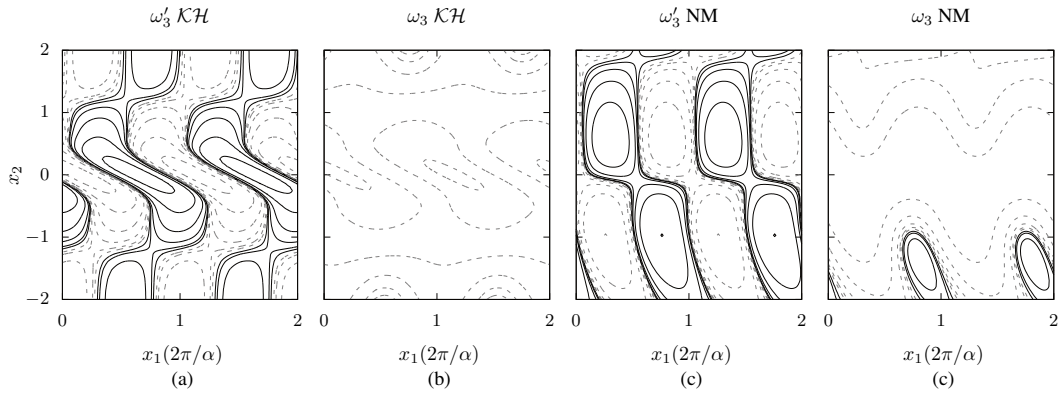

Figure 10. Comparison of perturbation and total fields of streamwise vorticity between the $\mathcal{KH}$ mode and the new mode.

7. SUMMARY AND CONCLUSIONS

A temporal linear stability analysis of a stratified shear flow under action of two scalar volume fractions has been performed in order to investigate the effect of settling particles on the instabilities developed. This analysis was based in linearised equations of continuity, Navier-Stokes and scalar transport, Boussinesq approximation and modal perturbation model with invariant basic state over the time. A computational code based in Chebyshev approximation, for the spatial derivatives, and *QZ* algorithm, to solve the eigenvalue problems, has been developed in *Julia language*. The validation of this code is achieved with results available in the literature.

The settling particles presence have basically two effects on the flow: a variation in the phase velocity and a deformation on the sediment concentration perturbation field of the $\mathcal{KH}$ mode, and amplifying more the new growth mode than the $\mathcal{KH}$ mode for some combinations of parameters (settling velocity, salinity Richardson number and density ratio). These variations in the $\mathcal{KH}$ mode can propitiate the growth of secondary instabilities. While the new mode have a different vortex dynamic.

For the full paper, we propose to extend this study to more values of settling velocity and salinity Richardson number and a more deep analysis of the new growth mode.

8. ACKNOWLEDGMENTS

The authors are grateful to Petrobras for supporting this research.

9. REFERENCES

Anderson, E., Bai, Z., Bischof, C., Blackford, L. S., Demmel, J., Dongarra, J. J., Du Croz, J., Hammarling, S., Greenbaum, A., McKenney, A., and Sorensen, D. (1999). *LAPACK Users' Guide (Third Ed.)*. Society for Industrial and Applied Mathematics, Philadelphia, PA, USA.

Baltensperger, R. and Trummer, M. R. (2003). Spectral differencing with a twist. *SIAM J. Sci. Comp.*, 24(5):1465–1487.

Berrut, J.-P. and Mittelmann, H. D. (2004). Adaptive point shifts in rational approximation with optimized denominator. *Journal of Computational and Applied Mathematics*, 164165(0):81 – 92.

Betchov, R. and Szewczyk, A. (1963). Stability of a shear layer between parallel streams. *The physics of fluids*, 6(10):1391 – 1396.

Burns, P. and Meiburg, E. (2012). Sediment-laden fresh water above salt water: linear stability analysis. *Journal of Fluid Mechanics*, 691:279–314.

Canuto, C., Hussaini, M. Y., Quarteroni, A., and Zang, T. A. (1988). *Spectral methods in fluid dynamics*. Springer series in computational physics. Springer-Verlag.

Hazel, P. (1972). Numerical studies of the stability of inviscid stratified shear flows. *Journal of Fluid Mechanics*, 51:39–61.

Horner-Devine, A. R., Hetland, R. D., and MacDonald, D. G. (2015). Mixing and transport in coastal river plumes. *Annual Review of Fluid Mechanics*, 47(1):569–594.

Julien, P. Y. (1998). *Erosion and sedimentation*. Cambridge University Press.

Juniper, M. P., Hanifi, A., and Theofilis, V. (2014). Modal stability theory. *Applied Mechanics Review*, 66(2):024804–.

Khavasi, E., Firoozabadi, B., and Afshin, H. (2014). Linear analysis of the stability of particle-laden stratified shear layers. *Canadian Journal of Physics*, 92(2):103–115.

Ortiz, S., Chomaz, J.-M., and Loiseleux, T. (2002). Spatial holmboe instability. *Phys. Fluids*, 14(8):2585–2597.

Parsons, J. D., Bush, J. W., and Syvitski, J. P. (2001). Hyperpycnal plume formation from riverine outflows with small sediment concentrations. *Sedimentology*, 48(2):465–478.

Schmid, P. J. and Brandt, L. (2014). Analysis of fluid systems: Stability, receptivity, sensitivity. *Applied Mechanics Reviews*, 66.

Squire, H. B. (1933). On the stability for three-dimensional disturbances of viscous fluid flow between parallel walls. *Proceedings of the Royal Society of London A: Mathematical, Physical and Engineering Sciences*, 142(847):621–628.

Weideman, J. A. and Reddy, S. C. (2000). A matlab differentiation matrix suite. *ACM Trans. Math. Softw.*, 26(4):465–519.